



Quantitative reconstruction of atomic orbital densities of neon from partial cross sections

Hans Kirschner ^{*}, Alexander Gottwald , Victor Soltwisch , and Mathias Richter 
Physikalisch-Technische Bundesanstalt, 10587 Berlin, Germany

Peter Puschnig 
Institute of Physics, NAWI Graz, University of Graz, 8010 Graz, Austria

Simon Moser 
Physikalisches Institut and Würzburg-Dresden Cluster of Excellence ct.qmat, Universität Würzburg, 97074 Würzburg, Germany

 (Received 26 May 2023; revised 22 September 2023; accepted 6 November 2023; published 23 January 2024)

The approach of photoemission orbital tomography, i.e., the orbital density reconstruction from photoemission of planar molecular layers by using a formalism equivalent to a Fourier transformation, is transferred to free atoms. Absolute radial orbital densities of neon $1s$, $2s$, and $2p$ orbitals are reconstructed with a central-field one-electron model, using well-known atomic photoionization data. The model parameters are optimized by a Markov chain Monte Carlo method with Bayesian inference from which uncertainties for the reconstructed orbital densities are derived. The presented model opens the path for photoemission orbital tomography as a powerful tool, as well as for a quantitative analysis.

DOI: [10.1103/PhysRevA.109.012814](https://doi.org/10.1103/PhysRevA.109.012814)

I. INTRODUCTION

Photoemission orbital tomography (POT) enables the reconstruction of real-space molecular orbitals from electron distributions in momentum space [1]. Within the one-step model of photoemission and the dipole approximation, the process is described as the transition from an initial state of the electron to its final state. In POT, the former is a molecular orbital and the latter describes the ejected photoelectron as a plane wave (PW), i.e., an electron propagating in free space. This approach was already suggested by Gadzuk [2] to calculate the photoemission angular distribution from molecular monolayers by a simplistic Fourier transformation of the initial molecular orbital.

Puschnig *et al.* [1] applied this approach to two-dimensional (2D) angular-dependent momentum space data (along k_x and k_y) from photoemission to reconstruct the 2D molecular orbitals. This idea was subsequently extended by a phase recovery [3–6] and a reconstruction in three dimensions (from data along k_x , k_y , and k_z) [7,8].

The method has led to convincing results, but has been criticized mainly for ignoring final-state scattering and the spherical wave nature of the emission [9]. The PW assumption leads further to an angular dependence proportional to \cos^2 , which falsely predicts the photoemission perpendicular to linearly polarized light [10]. Additionally, the PW cannot explain features along the k_z axis, as already seen in the previously

mentioned publications regarding the 3D reconstruction [7,8]. This problem was recently discussed in more detail by Kern *et al.* [11].

Further, POT has been initially limited to relative measurements in arbitrary units. Experimental photoemission intensities are commonly difficult to determine on an absolute scale, due to complex spectrometer techniques. Thus, qualitative statements about orbital density distributions can be made, but an absolute quantification with reliable uncertainties is not yet possible. To introduce such a quantification, the reconstruction method needs to be applied to absolute photoemission data. In this paper, we transfer the POT formalism to the reconstruction of atomic orbitals from gas-phase photoemission data of neon, which are known from the literature [12–15]. Similar to molecular layers, the photoemission from atoms in the gas phase is calculated via the matrix element, which describes the transition from the bound electron state of an atomic orbital to its final state as a photoelectron. Thus a similar reconstruction of initial atomic orbitals should be possible from measured differential partial cross sections, giving the angular- and energy-dependent photoemission on an absolute scale.

Differential partial cross sections for atomic photoionization have already been calculated. This includes approaches like Hartree-Fock [16], relativistic random-phase approximation [17], Hartree-Fock-Slater [18,19], and the R -matrix methods [20–22], the latter with usable implementations [23–26]. However, the inverse calculation, that is, the reconstruction of atomic orbital densities from cross section data, has not been reported in the literature so far. Here we present a method for reconstructing radial atomic orbital densities from partial cross section (PCS) data from the literature of neon on an absolute scale, which also allows us to consider resulting uncertainties quantitatively. The method is related to publications of McGuire [27,28], Manson and Cooper [29],

^{*}hans.kirschner@ptb.de

Published by the American Physical Society under the terms of the [Creative Commons Attribution 4.0 International license](https://creativecommons.org/licenses/by/4.0/). Further distribution of this work must maintain attribution to the author(s) and the published article's title, journal citation, and DOI.

Goldberg *et al.* [30], and Yeh and Lindau [18,19], calculating the PCS with one-electron wave functions in the dipole and central field of a Coulomb potential. Calculations based on these assumptions produce relatively accurate results for light atoms like neon, where many-electron correlation and relativistic effects are less pronounced [17,31–33]. The approach is thus also justified for even lighter atoms, such as H, C, or O, of which mainly also the molecules in POT are composed. A possible *a priori* estimation of the limits of the method can be formulated from the Hamiltonian for an N -electron atom. In the central-field approximation it can be written as [34–36]

$$\hat{H} = \sum_{i=1}^N \left(-\frac{\hbar}{2m} \nabla_i^2 + V_c(\mathbf{r}_i) \right) + V_r. \quad (1)$$

Here V_c is the potential of the central field. The potential V_r describes the residual interaction, which considers nonspherical parts. The criterion for the central-field approximation then is

$$\sum_{i=1}^N |V_c(\mathbf{r}_i)| \gg |V_r|, \quad (2)$$

where V_r is a minor perturbation and can be neglected.

By employing a Bayesian inference based on Markov chain Monte Carlo (MCMC) algorithms, we demonstrate the feasibility of determining orbital densities with robust uncertainty estimations.

The goals of the present work can be summed up as follows. In POT, the PW serves as an intuitive but simplistic approximation for the final state. It gives rise to the orbital reconstruction by a Fourier transformation, but *only* on a relative scale. We therefore aim to establish a quantifiable reconstruction process as a proof of principle on a system where reliable experimental data are available and the final state may be controlled. Atomic gases, like neon, meet these criteria. The photoemission from gas-phase atoms is free from final-state scattering and its description demands that we consider the spherical wave nature of the process and thus naturally avoids the PW. In this respect, our approach addresses the above-mentioned criticisms against POT and gives the possibility to examine the initial state and the final state beyond the PW assumption.

II. THEORETICAL DESCRIPTION AND MODEL

Our description of the photoemission cross section starts with Fermi's golden rule in terms of many-electron initial and final states Ψ_i^N and Ψ_f^N , respectively. The transition probability $W_{i \rightarrow f}$ from the initial ground state with energy E_i to the final state is given by [37]

$$W_{i \rightarrow f} = \frac{2\pi}{\hbar} |\langle \Psi_f^N | \mathbf{A} \mathbf{P} | \Psi_i^N \rangle|^2 \delta(\hbar\omega + E_i - E_f). \quad (3)$$

Here we use the dipole approximation in the velocity gauge with \mathbf{A} and \mathbf{P} the vector potential of the incoming light field and the electrons' momentum operator, respectively. We then approximate the final state by an antisymmetrized product between the ionized state $\Psi_{f,j}^{N-1}$ and the single-electron state ψ_f^k of the outgoing electron with momentum \mathbf{k} . This approximation neglects possible correlations between the photoelectron and the remaining $N-1$ electrons. Further, we introduce the Dyson orbital $\psi_j(\mathbf{r})$ as an overlap between the initial

N -electron state and the ionized state $\Psi_{f,j}^{N-1}$ [37,38],

$$\psi_j(\mathbf{r}) = \sqrt{N} \int d^3r_2 \cdots d^3r_N \times \overline{\Psi}_i^N(\mathbf{r}, \mathbf{r}_2, \dots, \mathbf{r}_N) \Psi_{f,j}^{N-1}(\mathbf{r}_2, \dots, \mathbf{r}_N). \quad (4)$$

Thus, the differential PCS of atoms in the gas phase can be interpreted as a single-electron matrix element between a one-electron initial state ψ_{nl} , which is in fact a Dyson orbital describing the ionization of the state $j = (nl)$, and the final state ψ_f^k . We switch to the length gauge and arrive at the expression [19]

$$\frac{d}{d\Omega} \sigma_{nl}(h\nu) = \frac{4\pi^2\alpha}{3} h\nu |\hat{\epsilon} \langle \psi_f^k | \hat{r} | \psi_{nl} \rangle|^2, \quad (5)$$

which describes the angular- and energy-dependent cross section for photoionization, where $\hat{\epsilon}$ is the polarization vector, α the fine-structure constant, and $h\nu$ the photon energy. For linearly polarized radiation along the z axis, the matrix element in Eq. (5) can be separated into radial and angular parts

$$\hat{\epsilon}_z \langle \psi_f^k | \hat{r} | \psi_{nl} \rangle = \langle kl' | r | nl \rangle \langle l'm' | C_0^1 | lm \rangle. \quad (6)$$

The quantum numbers of the final and initial states are connected by the dipole selection rules $l' = l \pm 1$ and $m' = m$. The first part in Eq. (6) defines the intensity and the energy dependence of the PCS. The second describes the angular dependence. Summing over all final states, averaging over all initial states [39], and focusing on the radial part, the energy-dependent PCS becomes [18,19,29,40]

$$\sigma_{nl}(h\nu) = \frac{4\pi^2\alpha a_0^2}{3} \frac{N_{nl}}{2l+1} h\nu \times [I_{l-1}^2(k) + (l+1)I_{l+1}^2(k)]. \quad (7)$$

Here a_0 is the Bohr radius, N_{nl} is the number of electrons in each subshell nl , and k is the momentum of the photoelectron. Equation (7) contains the one-electron radial dipole matrix elements $R_{l\pm 1}(k)$, which are expressed by

$$I_{l\pm 1}(k) = \int_0^\infty R_{l\pm 1}(kr) r R_{nl}(r) r^2 dr. \quad (8)$$

This is an integral transformation, which transforms the initial state $R_{nl}(r)$ from real space r to reciprocal space k , using the final state $R_{l\pm 1}(kr)$ as a kernel. Additionally, the radial parts of the dipole length r and the volume element in spherical coordinates r^2 are included. In the following, the final and the initial states are introduced to generate a model function $\sigma_{nl}^{\text{model}}(h\nu)$ for Eq. (7) that can be fitted to experimental data $\sigma_{nl}^{\text{expt}}(h\nu)$.

A. Final state

The photoionization process results in a photoelectron, which moves in the Coulomb field of the remaining photoion. For an unbound photoelectron, the solution to the radial Schrödinger equation with a Coulomb potential V_C is given by a Coulomb wave [41–43]

$$C_l(kr, Z_C) = N(k) e^{\pi Z_C / 2k} \frac{|\Gamma(l+1 - iZ_C/k)|}{(2l+1)!} \times (2kr)^l e^{-ikr} {}_1F_1(l+1 + iZ_C/k, 2l+2, 2ikr). \quad (9)$$

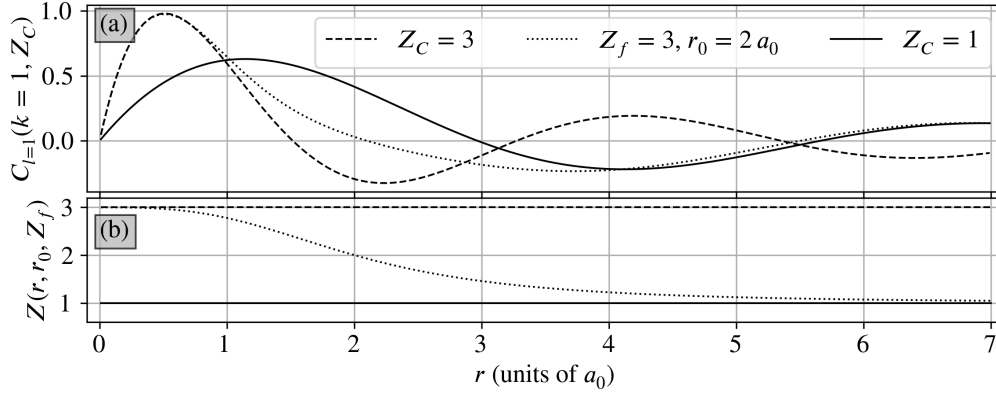


FIG. 1. (a) Coulomb wave functions $C_{l=1}(k=1, Z_C)$ as a function of the nuclear distance r given in atomic units for $Z_C = \text{const} = 3$ and 1, as well as for $Z_f = 3$ and $r_0 = 2a_0$, according to Eq. (11). For higher charge values, the wave function is drawn towards the core ($r=0$) values. For $r_0 = 2a_0$ the transition from $Z_C = 3$ to $Z_C = 1$ is visible. (b) Associated charge Z_C .

Here ${}_1F_1$ is the confluent hypergeometric function of the first kind, which is the solution to Kummer's differential equation and connected to the radial Schrödinger equation for a Coulomb potential $V_C \propto Z_C/r$ with constant charge Z_C . For $Z_C = 0$ the Coulomb wave equals a spherical Bessel function $j_l(kr)$, which is the solution of the radial Schrödinger equation for a free electron. In the continuous spectrum, wave functions are normalized for each k according to [44] via

$$\int_0^\infty r^2 dr C_l(kr) C_l(k'r) = \delta(k - k'). \quad (10)$$

Due to the multielectron configuration, a screened central potential $V_S \propto Z(r)/r$ is a better choice to describe the field than a Coulomb potential V_C with a constant charge Z_C . We approximate the solution to the Schrödinger equation with such a screened potential by setting the charge in Eq. (9) as a function of r such that $Z_C \rightarrow Z(r)$. Near the origin at $r \rightarrow 0$, it can be assumed the final state depends on a charge Z_f similar to the proton number with deviations due to screening effects. Far away from the single ionized atom, the electron will see a charge of 1. In the following, we will use

$$Z(r, r_0, Z_f) = Z_f - \frac{Z_f - 1}{(1 + \frac{r_0}{r})^3} = \frac{Z_f + (\frac{r}{r_0})^3}{1 + (\frac{r}{r_0})^3}, \quad (11)$$

which satisfies the asymptotic conditions and becomes, moreover, $Z_f - (Z_f - 1)(r/r_0)^3$ for $r \ll r_0$. This is the exact solution for a homogeneously charged sphere of radius r_0 .

The shape of $Z(r, r_0, Z_f)$ changes the course of the Coulomb wave. In Fig. 1(a), examples of $C_{l=1}$ for constant charges $Z_C = 3$ and 1 are shown. For $Z_C = 3$, the charge distribution is drawn towards $r=0$, compared to $Z_C = 1$. Additionally, $Z(r, r_0 = 2a_0, Z_f = 3)$ according to Eq. (11) shows the transition between these two values with the required asymptotic values of $Z(r)$ [see Fig. 1(b)]. The parameter r_0 describes the rate at which the charge and therefore the Coulomb potential $V_S \propto Z(r)/r$ changes along the radius. Summing up, the final state introduces two parameters r_0 and Z_f .

B. Initial state

For the initial state, a linear combination of Slater-type orbitals (STOs) is introduced [45–48] with adjustable parameters of amplitude A_g and charge Z_i . These parameters are propagated through the integral transformation in Eq. (8) and fitted to experimental data. The linear combination of STOs is written as

$$R_{nl}(r, A_g, Z_i) = \sum_{g=0}^{n-1-l} A_g r^{g+l} e^{-rZ_i/n}. \quad (12)$$

In this paper radial wave functions $1s$, $2s$, and $2p$ are used, leading to

$$R_{10}(r, A_0, Z_i) = A_0 e^{-rZ_i}, \quad (13)$$

$$R_{20}(r, A_0, A_1, Z_i) = (A_0 + A_1 r) e^{-rZ_i/2}, \quad (14)$$

$$R_{21}(r, A_0, Z_i) = A_0 r e^{-rZ_i/2}. \quad (15)$$

For the $2s$ state a phase change is encoded in the amplitude parameters A_g by a change of sign leading to $A_0 < 0 < A_1$ or vice versa $A_1 < 0 < A_0$. This ambiguity is due to the absolute square in Eq. (5). We set $A_0 > 0$ as a convention. The functions are normalized via

$$\int_0^\infty R_{nl}^2(r, A_g, Z_i) r^2 dr = 1. \quad (16)$$

The initial state introduces the parameters A_g and Z_i . Along with the final state, the radial integral transformation in Eq. (8) is thus fully described and used in Eq. (7) to generate the model function $\sigma_{nl}^{\text{model}}(h\nu, [r_0, Z_f, A_g, Z_i])$ with fitting parameters in square brackets. This model is optimized against the experimental data $\sigma_{nl}^{\text{expt}}(h\nu)$ to estimate the best set of parameters, which will be explained in the next section.

III. OPTIMIZATION METHODS

A. Range scan for the final-state parameters r_0 and Z_f

With the fit parameters r_0 , Z_f , A_g , and Z_i , the radial integral from Eq. (8) becomes

$$I_{l\pm 1}(k) = \int_0^\infty C_{l\pm 1}(kr, Z(r, r_0, Z_f)) r^2 R_{nl}(r, A_g, Z_i) dr. \quad (17)$$

We will numerically evaluate this integral transformation. Its computation time scales linearly with the number of measurement points in reciprocal space (k space). For each point in k space, it is necessary to calculate the normalization constant $N(k)$ from Eq. (10), each with a specific extent and precision in real space (r space). This is due to the oscillation frequency of C_l , which increases for higher k and necessitates a higher precision in r . The most time consuming part in calculating C_l is the confluent hypergeometric function ${}_1F_1(a, b, z)$, which is evaluated with the PYTHON-FLINT package [49]. A single calculation of ${}_1F_1(a, b, z)$ takes about 50 μ s. To calculate the normalization constant $N(k)$ for one k point, we use about 20 000 grid points in r . For ten measurement points in k space this leads to about 10 s. However, to cover possible multimodalities and correlations in the reconstructed parameters r_0 , Z_f , A_g , and Z_i plus their uncertainties, we choose an MCMC-based Bayesian inference optimizer, which is briefly overviewed in the next section. Typically, an MCMC algorithm relies on calling a model function many thousand times. The number of calls is specifically given by a number of so-called walkers and the amount of steps each walker takes. For a comparatively small number of ten walkers, each taking 1000 steps, the model function is called 10 000 times. With the 10 s from one iteration this leads to a calculation time of more than one day for only ten measurement points, which is impractical. Additional overheads are not even included in this estimate. One way to reduce the calculation time is to exclude the parameters r_0 and Z_f from the MCMC method and scan them in fixed ranges. For five steps in r_0 and five steps in Z_f , the normalization of $C_l(kr, Z(r, r_0, Z_f))$ only needs to be calculated 25 times, leading to an estimated computational time of only approximately 5 s. As a tradeoff, the uncertainty determination was omitted for r_0 and Z_i . However, the parameters A_g and Z_i , which are finally used to reconstruct the absolute orbital density and their respective uncertainties, can be estimated by the MCMC method, which is briefly introduced in the next section.

B. MCMC-based Bayesian inference for the initial-state parameters A_g and Z_i

The parameters Z_i and A_g are determined from experimental PCS data $\sigma_{nl}^{\text{expt}}(h\nu)$ by minimizing an objective (or loss) function, which compares the experimental data against a model function, in this case $\sigma_{nl}^{\text{model}}(h\nu, [A_g, Z_i])$. The process combines MCMC algorithms and Bayesian inferences. The latter allows for an extended investigation of the so-called posterior probability distribution of the model parameters A_g and Z_i and helps to indicate possible model problems, gauging convergence and uncovering multimodalities or parameter correlations. In general, with MCMC algorithms, the full

parameter space can be explored, while Bayesian inference links the updated probabilities from MCMC sampling to the determined parameters. In this study, sampler ensemble proposals are produced by the stretch move are employed, as proposed by Goodman and Weare [50]. The method was implemented in the EMCEE PYTHON package [51]. With Bayes' theorem, the posterior probability of the parameters \mathbf{p} given the measured data \mathbf{M} is proportional to

$$\mathcal{P}(\mathbf{p}|\mathbf{M}) \propto \mathcal{P}(\mathbf{M}|\mathbf{p}). \quad (18)$$

Here \mathbf{p} denotes the target parameters for this study $\mathbf{p} = [A_g; Z_i]$, while $\mathcal{P}(\mathbf{M}|\mathbf{p})$ represents the likelihood of obtaining data \mathbf{M} given the parameters \mathbf{p} . For the experimental PCS, we used neon literature data lacking uncertainties, which however are necessary for the presented method. To address this, an uncertainty model $u(h\nu)$ is introduced, summing relative and absolute contributions to mimic uncertainties under 10%. Assuming uncorrelated Gaussian distributed uncertainties $u(h\nu)$, the likelihood function comparing the experimental PCS $\sigma_{nl}^{\text{expt}}(h\nu)$ and the model $\sigma_{nl}^{\text{model}}(h\nu, [A_g, Z_i])$ is given by

$$\mathcal{P}(\mathbf{M}|\mathbf{p}) = \prod_{h\nu} \frac{1}{\sqrt{2\pi u^2(h\nu)}} \times \exp\left(-\frac{\{\sigma_{nl}^{\text{model}}(h\nu, [A_g, Z_i]) - \sigma_{nl}^{\text{expt}}(h\nu)\}^2}{2u^2(h\nu)}\right). \quad (19)$$

The product is evaluated over all experimental data points along $h\nu$. Further details on this method can be found in other works [52–56] in various physical contexts. The result of this optimization approach is the approximated posterior probability distribution of the parameters $\mathbf{p} = [A_g; Z_i]$, from which best values and uncertainties can be extracted.

IV. RESULTS

In this section we present the results for the parameters Z_f and r_0 , as well as A_g and Z_i , derived from the optimization described in Sec. III. To compare with experimental data, the best values are put into the model function $\sigma_{nl}^{\text{model}}$ and plotted alongside the data of neon $1s$, $2p$, and $2s$ in Figs. 4(b), 5(b), and 6(b), respectively. Orbital electron densities are reconstructed by inserting the best values for A_g and Z_i in the initial wave functions from Eq. (12), presented in Figs. 4(a), 5(a), and 6(a). These densities are compared with Hartree-Fock (HF) calculations by Worsley [57], serving as an *ad hoc* comparison to self-consistent fields for the neon $1s^2 2s^2 2p^6$ electron configuration.

A. Scanning Z_f and r_0

As described in Sec. III, the parameters Z_f and r_0 of C_l are scanned in fixed ranges. For neon $1s$ the results are plotted in a heatmap in Fig. 2 for each combination of r_0 and Z_f . The size of each rectangle corresponds to the likelihood, which is measured on a relative scale. Explicit values are therefore not presented. We just aim for a maximum likelihood and thus for biggest rectangle area. This is the case for $r_0 = 5$.

Another important figure of merit is the normalization of the initial radial wave function $R_{nl}(r, A_g, Z_i)$. It should be

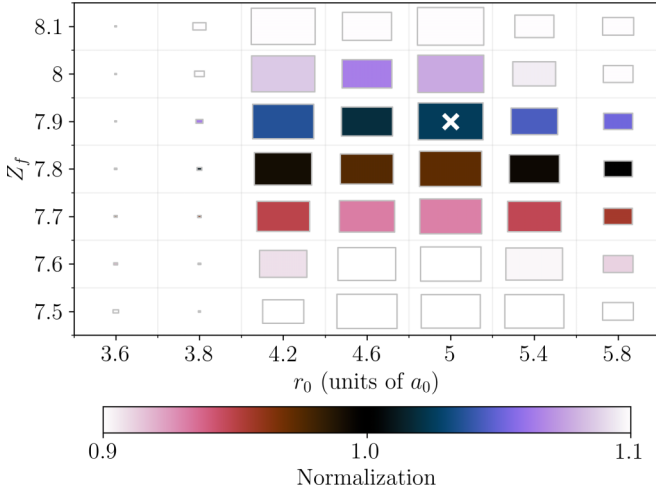


FIG. 2. Heatmap of the fit results for the parameters Z_f and r_0 of the neon $1s$ orbital with color encoded normalization and size encoded likelihood. The best result is achieved at ($Z_f = 7.9$, $r_0 = 5a_0$) and marked by a white cross.

equal to 1 and enforcing this using Eq. (16) would have been one possible way. However, also the MCMC algorithm allows us to implement such a normalization by using constraints. Without this constraint multimodalities in $\sigma_{nl}^{\text{model}}$ can be detected. These may be helpful to indicate possible model errors and ruling them out. For neon $1s$ and $2s$, we constrained the normalization to a range of 0.8–1.2. For neon $2p$, such a constraint was found not to be necessary, which confirms the validity of the implemented model. In Fig. 2, the normalization is encoded in the color scheme, with black equal to 1 and deviations going to white. The aforementioned constraint from 0.8 to 1.2 was narrowed to 0.9 and 1.1 for better visibility. Including the normalization for assessing the best choice of parameters, a value for Z_f between 7.8 and 7.9 can be identified. We chose $Z_f = 7.9$ and marked it together with $r_0 = 5$ in Fig. 2 by a white cross.

The heatmaps for neon $2p$ and neon $2s$ are omitted here, but the results for Z_f and r_0 are summarized in Table I. The decreasing r_0 along $1s \rightarrow 2s \rightarrow 2p$ reflects the increasing screening of the nuclear charge by core electrons. Table I also shows the fit results for Z_i , which will be explained in more detail in the following section. From a physical point of view one may expect $Z_i = Z_f$, since shortly after photoemission the photoelectron should experience the same charge as in the bound state. This coupling of Z_i and Z_f would have been contrary to our attempt to stay within reasonable computing times, as explained in Sec. III. However, it can be seen that $Z_i \approx Z_f$, which speaks in favor of our applied model.

TABLE I. Results for the final charge Z_f , the radial extension r_0 , and the reconstructed initial charge Z_i for neon $1s$, $2s$, and $2p$.

Parameter	$1s$	$2s$	$2p$
$r_0 (a_0)$	5.0	4.2	2.6
Z_f	7.9	4.3	4.7
Z_i	7.4	5.94	6.08

B. Probability distributions for A_g and Z_i

In the following, the MCMC solution is presented for neon $1s$, $2s$, and $2p$ for each parameter set Z_f and r_0 from Table I. First, so-called corner plots are shown, including the posterior probability distributions of the parameters A_g and Z_i , as well as their correlations. These plots were made with the PYTHON module `corner.py` [58]. Furthermore, the reconstructed initial radial atomic wave function and the fit result for the PCS are presented with uncertainty contributions.

1. Neon $1s$

For neon $1s$, two parameters A_0 and Z_i are fitted, according to Eq. (13). The MCMC results are shown in Fig. 3(a). Both parameters are normally distributed and positively correlated. This correlation relates to the normalization constraint in Eq. (16) to $Z_i = (A_0/2)^{3/2}$. The dashed lines mark probabilities (p values) of 16% and 84%, which equal 1σ standard deviation in the case of a normal distribution. The mean value ($p = 50\%$) is marked with a line and projected onto the 2D plot. The fit results are $A_0 = 40.9 \pm 0.6$ and $Z_i = 7.4 \pm 0.1$.

These values are used together with Eq. (13) to reconstruct the initial radial orbital density $(rR)^2$, which is plotted in Fig. 4(a). In Fig. 4(b), the experimental PCS data from Saito and Suzuki [12] with the fit result are shown.

In addition to our results, we plot the HF calculated wave function of neon $1s$ from Worsley [57]. The HF calculations show good agreement with the presented result, with both maximum positions being around $r = 0.115a_0$. The overall shape of the wave function is shifted towards $r = 0$, indicating a different Z_i .

For both Figs. 4(a) and 4(b), the results are generated from the mean values of the histograms for A_0 and Z_i in Fig. 3(a). The fit result is in good agreement with the experimental data. In Fig. 4(c), the p values from Fig. 3(a) are translated to the uncertainty range $\Delta_{(rR)^2}$ with values of two magnitudes smaller than the orbital density. In Fig. 4(d), a similar plot is shown, but now in reciprocal space. The dashed line shows the uncertainty range Δ_σ from the fit result of the PCS in Fig. 4(b). Also the experimental data are shown as a deviation from the fit result from Fig. 4(b). The dotted zero line in Figs. 4(c) and 4(d) equals the mean fit result from Figs. 4(a) and 4(b), respectively.

2. Neon $2p$

The initial wave function of neon $2p$ is constructed from Eq. (15) with two parameters A_0 and Z_i , in analogy to neon $1s$. The corner plot with histograms for the parameter distributions of A_0 and Z_i is shown in Fig. 3(c). Both histograms exhibit a normal distribution, with a positive correlation between the two parameters, similar to neon $1s$. This behavior can again be attributed to the preservation of the normalization. The fit results for neon $2p$ are shown in Fig. 5. Experimental data were taken from Marr and West [59] and Wulleumier and Krause [14,15]. Again, the lines in Figs. 5(a) and 5(b) give the radial orbital density $(rR_{21})^2$ and the PCS, respectively, generated from the mean values from the distributions of the fitted parameters A_0 and Z_i in Fig. 3(c). The fit of the PCS in Fig. 5(b) follows the general shape of the experimental data.

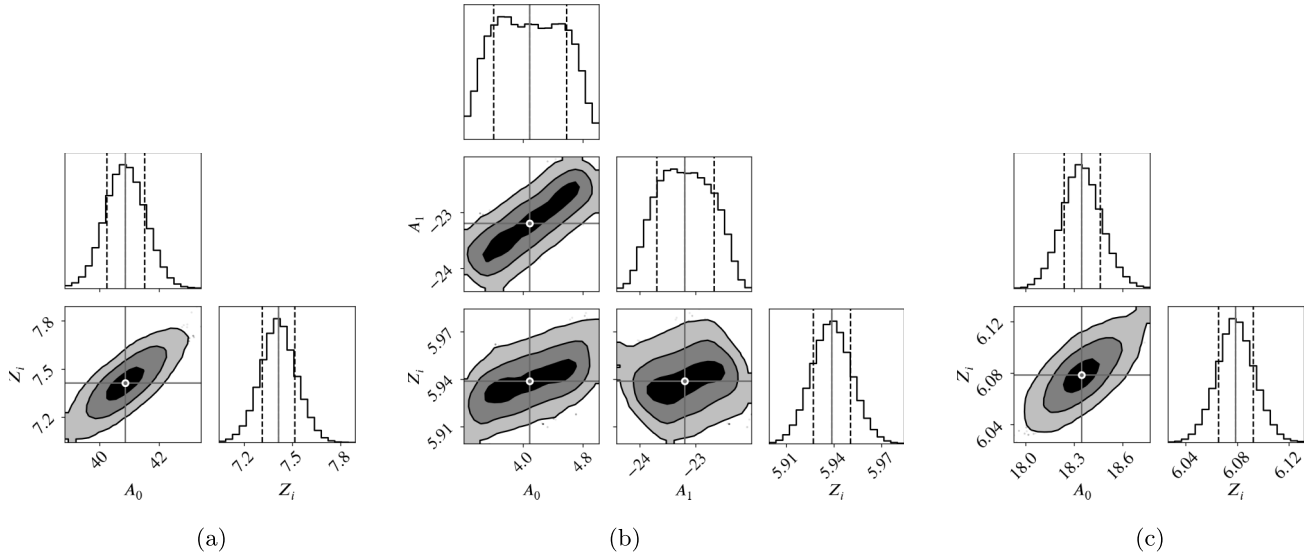


FIG. 3. Corner plots for neon (a) $1s$, (b) $2s$, and (c) $2p$ with fit results and uncertainties for the parameters (a) $A_0 = 40.9 \pm 0.6$ and $Z_i = 7.4 \pm 0.1$, (b) $A_0 = 4.1 \pm 0.5$, $A_1 = -23.2 \pm 0.5$, and $Z_i = 5.94 \pm 0.01$, and (c) $A_0 = 18.3 \pm 0.1$ and $Z_i = 6.08 \pm 0.01$.

A radial orbital density can be reconstructed with the approach introduced here [see Fig. 5(a)]. Again, we plotted the HF calculated wave function of neon $2p$ from [57]. The maximum position shows even better agreement with our result at about $r = 0.65a_0$ than for neon $1s$. The overall center is slightly shifted towards higher- r values. The uncertainty range shown in Fig. 5(c) is gained from the histograms in Fig. 3(c) and is about three orders of magnitude smaller than the actual density.

3. Neon 2s

The fit method was also applied to neon $2s$ with its three fit parameters A_0 , A_1 , and Z_i , according to Eq. (14). The distribution of each parameter is shown in Fig. 3(b). Again, the charge parameter Z_i follows a normal distribution. The pa-

rameter A_0 follows a smoothed uniform distribution. Also, the parameter A_1 follows a normal distribution, which is slightly broadened. The behavior of A_0 and A_1 can be explained by looking at Fig. 6(a). The first maximum at $r \approx 0.1a_0$ of the radial orbital density is mainly influenced by the amplitude parameter A_0 . The resulting maximum is small compared to the second maximum at $r \approx 0.8a_0$, which is mainly defined by A_1 . As mentioned above, the normalization of the orbital density is limited to values between 0.8 and 1.2. Thus, the shape of $(rR)^2$ varies within this limits. Any change of A_0 has only a small influence on the normalization value and is additionally compensated by a minor change in A_1 , hence the resulting smoothed uniformlike distribution of A_0 . The slight broadening of the normal distribution of A_1 can be explained in the same way.

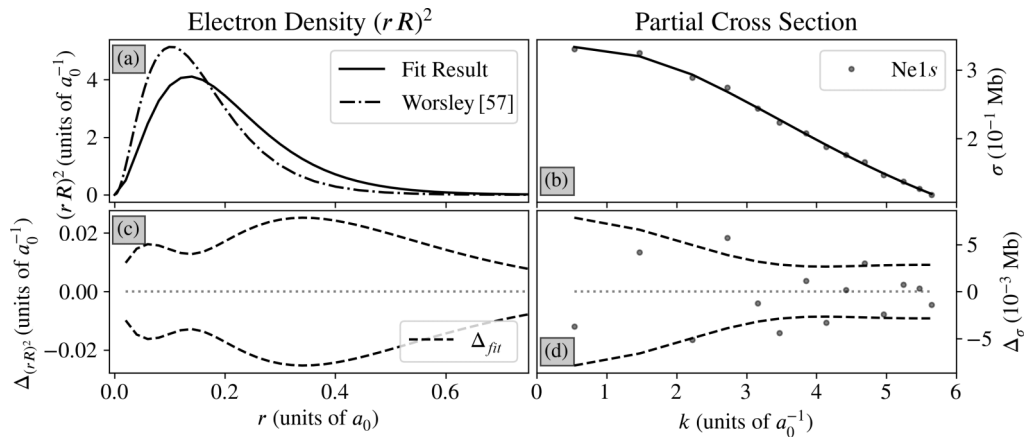


FIG. 4. Neon $1s$ result for $r_0 = 5a_0$ and $Z_f = 7.9$ with experimental data from Saito and Suzuki [12]. (a) Reconstructed radial orbital density $(rR)^2$. Additionally, the Hartree-Fock solution is shown as a comparison, as calculated by Worsley [57]. (b) Fit result for the PCS, which is in good agreement with the experimental data (\bullet). (c) Uncertainty range of the radial orbital density, generated from the distributions in Fig. 3(a). (d) Uncertainty range from the fit result of the PCS, marked by the dashed line and the deviation from the experimental values (\bullet).

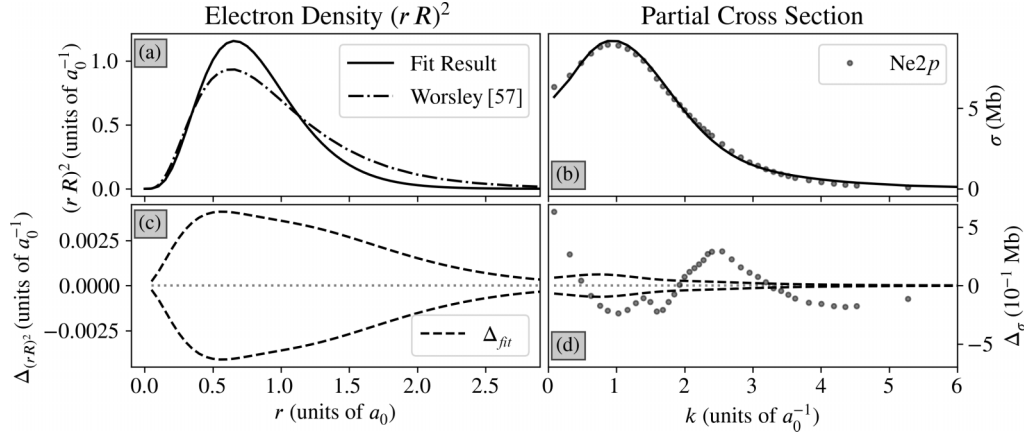


FIG. 5. Neon $2p$ results for $Z_f = 4.7$ and $r_0 = 2.6a_0$ with experimental data merged from Marr and West [59] and Wuilleumier and Krause [14,15]. (a) Reconstructed radial orbital density $(rR)^2$. Additionally, the Hartree-Fock solution is shown as a comparison, as calculated by Worsley [57]. (b) Fit result for the PCS, which is in good agreement with the experimental data (\bullet). (c) Uncertainty range of the radial orbital density, generated from the distributions in Fig. 3(c). (d) Uncertainty range from the fit result of the PCS, marked by the dashed line and the deviation from the experimental values (\bullet).

The reconstructed radial orbital density is shown in Fig. 6(a). Figure 6(b) shows the fit result and the experimental data, which were taken from Wuilleumier and Krause [14,15]. Figure 6(d) shows the uncertainty range from the fit results in reciprocal space, marked by a dashed line.

V. CONCLUSION

We have applied the approach of reconstructing orbital density distributions to atomic $1s$, $2s$, and $2p$ orbitals of neon from experimental cross section data. For noble gases, such as neon, experimental data of partial cross sections are known on an absolute scale. Thus, also the orbital densities could be determined on an absolute scale with a well-founded uncertainty. For this purpose, the experimental data were fitted using a one-electron central-field model for the PCS. The fit parameters and uncertainty contributions were determined using an MCMC method with Bayesian inference.

In contrast to classical POT on planar molecular layers, photoemission from isolated atoms implies spherical symmetry and is free of final-state scattering. In this respect, our approach addresses major criticisms against POT [9,10]. Instead of a PW, a Coulomb wave with a screened potential was applied as the final state and showed convincing results.

The presented method might be improved by further expanding the number of parameters, i.e., Z_f and r_0 , for the MCMC procedure to specify their distributions, uncertainties, and general contributions to the reconstruction process. The assumption for the shape of $Z(r)$ in the final state may be optimized towards methods as used, for example, by Cooper and Manson [29,44]. Finally, the model used has the potential to be extended by more complex assumptions such as relativistic or many-electron correlation effects. Next steps also relate to the application of the method to molecular orbitals, both in the gas phase and on substrates within a planar geometry, to further test the POT and the PW assumption.

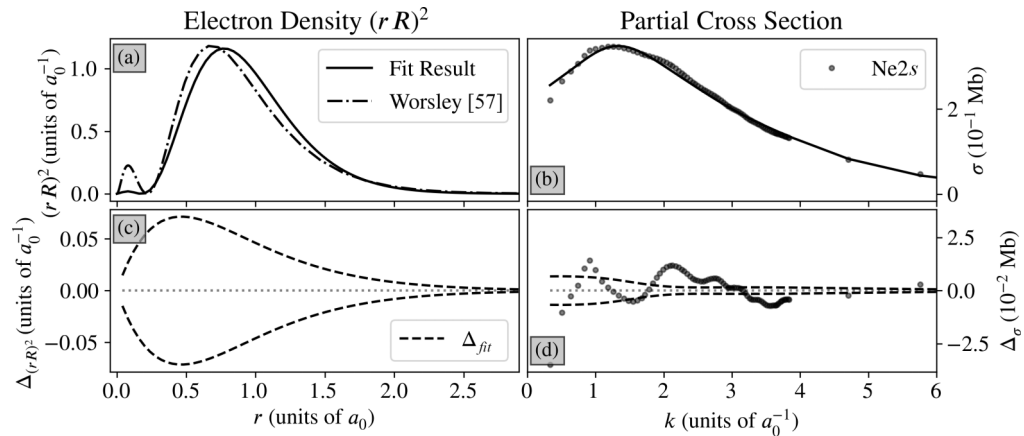


FIG. 6. Neon $2s$ results for $Z_f = 4.3$ and $r_0 = 4.2a_0$ with experimental data merged from Wuilleumier and Krause [14,15]. (a) Reconstructed radial orbital density $(rR)^2$. Additionally, the Hartree-Fock solution is shown as a comparison, as calculated by Worsley [57]. (b) Fit result for the PCS, which is in good agreement with the experimental data (\bullet). (c) Uncertainty range of the radial orbital density, generated from the distributions in Fig. 3(b). (d) Uncertainty range from the fit result of the PCS, marked by the dashed line and the deviation from the experimental values (\bullet).

ACKNOWLEDGMENTS

The authors thank Jens Viefhaus from the Helmholtz-Zentrum Berlin for contributing the digitized literature

data. This work was funded by the Exploring the Foundations of Photoemission Tomography project of the DFG Project No. 396769409 and FWF with Project No. I 3731, respectively.

-
- [1] P. Puschnig, S. Berkebile, A. J. Fleming, G. Koller, K. Emtsev, T. Seyller, J. D. Riley, C. Ambrosch-Draxl, F. P. Netzer, and M. G. Ramsey, *Science* **326**, 702 (2009).
- [2] J. W. Gadzuk, *Phys. Rev. B* **10**, 5030 (1974).
- [3] D. Lüftner, T. Ules, E. M. Reinisch, G. Koller, S. Soubatch, F. S. Tautz, M. G. Ramsey, and P. Puschnig, *Proc. Natl. Acad. Sci. USA* **111**, 605 (2014).
- [4] H. Offenbacher, D. Lüftner, T. Ules, E. M. Reinisch, G. Koller, P. Puschnig, and M. G. Ramsey, *J. Electron Spectrosc. Relat. Phenom.* **204**, 92 (2015).
- [5] P. Kliuiev, T. Latychevskaia, J. Osterwalder, M. Hengsberger, and L. Castiglioni, *New J. Phys.* **18**, 093041 (2016).
- [6] G. S. M. Jansen, M. Keunecke, M. Düvel, C. Möller, D. Schmitt, W. Bennecke, F. J. S. Kappert, D. Steil, D. R. Luke, S. Steil, and S. Mathias, *New J. Phys.* **22**, 063012 (2020).
- [7] S. Weiß, D. Lüftner, T. Ules, E. M. Reinisch, H. Kaser, A. Gottwald, M. Richter, S. Soubatch, G. Koller, M. G. Ramsey, F. S. Tautz, and P. Puschnig, *Nat. Commun.* **6**, 8287 (2015).
- [8] M. Graus, C. Metzger, M. Grimm, P. Nigge, V. Feyer, A. Schöll, and F. Reinert, *Eur. Phys. J. B* **92**, 80 (2019).
- [9] A. M. Bradshaw and D. P. Woodruff, *New J. Phys.* **17**, 013033 (2015).
- [10] N. V. Richardson, *Chem. Phys. Lett.* **102**, 390 (1983).
- [11] C. S. Kern, A. Haags, L. Egger, X. Yang, H. Kirschner, S. Wolff, T. Seyller, A. Gottwald, M. Richter, U. De Giovannini, A. Rubio, M. G. Ramsey, F. C. Bocquet, S. Soubatch, F. S. Tautz, P. Puschnig, and S. Moser, *Phys. Rev. Res.* **5**, 033075 (2023).
- [12] N. Saito and I. H. Suzuki, *Int. J. Mass Spectrom. Ion Process.* **115**, 157 (1992).
- [13] G. V. Marr and J. B. West, *Proc. R. Soc. London Ser. A* **349**, 397 (1976).
- [14] F. Wuilleumier and M. O. Krause, *Phys. Rev. A* **10**, 242 (1974).
- [15] F. Wuilleumier and M. Krause, *J. Electron Spectrosc. Relat. Phenom.* **15**, 15 (1979).
- [16] D. J. Kennedy and S. T. Manson, *Phys. Rev. A* **5**, 227 (1972).
- [17] W. R. Johnson and K. T. Cheng, *Phys. Rev. A* **20**, 978 (1979).
- [18] J. J. Yeh and I. Lindau, *At. Data Nucl. Data Tables* **32**, 1 (1985).
- [19] J. Yeh, *Atomic Calculation of Photoionization Cross-Sections and Asymmetry Parameters* (Gordon & Breach, Philadelphia, 1993).
- [20] K. Berrington, P. Burke, J. Chang, A. Chivers, W. Robb, and K. Taylor, *Comput. Phys. Commun.* **8**, 149 (1974).
- [21] K. T. Taylor, *J. Phys. B* **10**, L699 (1977).
- [22] P. G. Burke, *R-Matrix Theory of Atomic Collisions* (Springer, Berlin, 2011).
- [23] N. Scott and K. Taylor, *Comput. Phys. Commun.* **25**, 347 (1982).
- [24] K. A. Berrington, W. B. Eissner, and P. H. Norrington, *Comput. Phys. Commun.* **92**, 290 (1995).
- [25] J. Tennyson, D. B. Brown, J. J. Munro, I. Rozum, H. N. Varambhia, and N. Vinci, *J. Phys.: Conf. Ser.* **86**, 012001 (2007).
- [26] Z. Mašín, J. Benda, J. D. Gorfinkiel, A. G. Harvey, and J. Tennyson, *Comput. Phys. Commun.* **249**, 107092 (2020).
- [27] E. J. McGuire, *Phys. Rev.* **161**, 51 (1967).
- [28] E. J. McGuire, *Phys. Rev.* **175**, 20 (1968).
- [29] S. T. Manson and J. W. Cooper, *Phys. Rev.* **165**, 126 (1968).
- [30] S. M. Goldberg, C. S. Fadley, and S. Kono, *J. Electron Spectrosc. Relat. Phenom.* **21**, 285 (1981).
- [31] M. Y. Amusia and N. A. Cherepkov, *Case Stud. At. Phys.* **5**, 47 (1975).
- [32] W. R. Johnson and C. D. Lin, *Phys. Rev. A* **20**, 964 (1979).
- [33] W. R. Johnson, in *Advances in Atomic and Molecular Physics*, edited by D. R. Bates and B. Bederson (Elsevier, Amsterdam, 1989), Vol. 25, pp. 375–391.
- [34] M. Fox, *A Student's Guide to Atomic Physics* (Cambridge University Press, Cambridge, 2018).
- [35] I. V. Hertel and C.-P. Schulz, *Atome, Moleküle und Optische Physik 1: Atomphysik und Grundlagen der Spektroskopie* (Springer, Berlin, 2008).
- [36] J. Goldstone, *Proc. R. Soc. London Ser. A* **239**, 267 (1957).
- [37] M. Dauth, M. Wiessner, V. Feyer, A. Schöll, P. Puschnig, F. Reinert, and S. Kümmel, *New J. Phys.* **16**, 103005 (2014).
- [38] A. I. Krylov, *J. Chem. Phys.* **153**, 080901 (2020).
- [39] J. Cooper and R. N. Zare, in *Lectures in Theoretical Physics: Atomic Collision Processes*, edited by S. Geltman, K. Mahanthappa, and W. Brittin (Gordon and Breach, New York, 1969), Vol. 11C, p. 317.
- [40] S. T. Manson, in *Advances in Electronics and Electron Physics*, edited by L. Marton (Elsevier, 1976), Vol. 41, pp. 73–111.
- [41] H. Friedrich, *Theoretische Atomphysik* (Springer, Berlin, 1994).
- [42] S. Gozem, A. Gunina, T. Ichino, D. Osborn, J. F. Stanton, and A. I. Krylov, *J. Phys. Chem. Lett.* **6**, 4532 (2015).
- [43] L. D. Landau and E. M. Lifshitz, *Quantum Mechanics: Non-Relativistic Theory* (Elsevier, London, 1991).
- [44] J. W. Cooper, *Phys. Rev.* **128**, 681 (1962).
- [45] D. Belkić and H. S. Taylor, *Phys. Scr.* **39**, 226 (1989).
- [46] D. Calderini, S. Cavalli, C. Coletti, G. Grossi, and V. Aquilanti, *J. Chem. Sci.* **124**, 187 (2012).
- [47] *Springer Handbook of Atomic, Molecular, and Optical Physics*, edited by G. Drake (Springer, New York, 2006).
- [48] A. Förster and L. Visscher, *J. Chem. Theory Comput.* **17**, 5080 (2021).
- [49] The FLINT team, FLINT: Fast Library for Number Theory, <https://github.com/fredrik-johansson/python-flint/> (2023).
- [50] J. Goodman and J. Weare, *Commun. Appl. Math. Comput. Sci.* **5**, 65 (2010).
- [51] D. Foreman-Mackey, D. Hogg, D. Lang, and J. Goodman, *Publ. Astron. Soc. Pac.* **125**, 306 (2013).

- [52] D. Sivia and J. Webster, *Physica B* **248**, 327 (1998).
- [53] D. Sivia, W. David, K. Knight, and S. Gull, *Physica D* **66**, 234 (1993).
- [54] M. P. Hobson and J. E. Baldwin, *Appl. Opt.* **43**, 2651 (2004).
- [55] S. Sharma, *Annu. Rev. Astron. Astrophys.* **55**, 213 (2017).
- [56] S. Heidenreich, H. Gross, and M. Bar, *Int. J. Uncertain. Quant.* **5**, 511 (2015).
- [57] B. H. Worsley, *Can. J. Phys.* **36**, 289 (1958).
- [58] D. Foreman-Mackey, *JOSS* **1**, 24 (2016).
- [59] G. V. Marr and J. B. West, *At. Data Nucl. Data Tables* **18**, 497 (1976).